Quasifree Λ, Σ^0, and Σ^- electroproduction from ^{1,2}H, ^{3,4}He, and carbon

F. Dohrmann,[1,2,*] A. Ahmidouch,[3,4] C. S. Armstrong,[5,6] J. Arrington,[2] R. Asaturyan,[7] S. Avery,[3] K. Bailey,[2] H. Bitao,[3] H. Breuer,[8] D. S. Brown,[8] R. Carlini,[5] J. Cha,[3] N. Chant,[8] E. Christy,[3] A. Cochran,[3] L. Cole,[3] J. Crowder,[9] S. Danagoulian,[5,10] M. Elaasar,[11] R. Ent,[5] H. Fenker,[5] Y. Fujii,[12] L. Gan,[3] K. Garrow,[5] D. F. Geesaman,[2] P. Gueye,[3] K. Hafidi,[2] W. Hinton,[3] H. Juengst,[13] C. Keppel,[3] Y. Liang,[3] J. H. Liu,[13] A. Lung,[5] D. Mack,[5] P. Markowitz,[5,14] J. Mitchell,[5] T. Miyoshi,[12] H. Mkrtchyan,[7] S. K. Mtingwa,[10] B. Mueller,[2] G. Niculescu,[3,15] I. Niculescu,[3,16] D. Potterveld,[2] B. A. Raue,[5,14] P. E. Reimer,[2] J. Reinhold,[5,14] J. Roche,[6] M. Sarsour,[17] Y. Sato,[12] R. E. Segel,[18] A. Semenov,[4] S. Stepanyan,[7] V. Tadevosyan,[7] S. Tajima,[19] L. Tang,[3] A. Uzzle,[3] S. Wood,[5] H. Yamaguchi,[12] C. Yan,[4] L. Yuan,[3] B. Zeidman,[2] M. Zeier,[20] and B. Zihlmann[20]

[1]*Forschungszentrum Dresden-Rossendorf, D-01314 Dresden, Germany*
[2]*Argonne National Laboratory, Argonne, Illinois 60439, USA*
[3]*Hampton University, Hampton, Virginia 23668, USA*
[4]*Kent State University, Kent, Ohio 44242, USA*
[5]*Thomas Jefferson National Accelerator Facility, Newport News, Virginia 23606, USA*
[6]*College of William and Mary, Williamsburg, Virginia 23187, USA*
[7]*Yerevan Physics Institute, Yerevan, Armenia*
[8]*University of Maryland, College Park, Maryland 20742, USA*
[9]*Juniata College, Huntingdon, Pennsylvania 16652, USA*
[10]*North Carolina A&T State University, Greensboro, North Carolina 27411, USA*
[11]*Southern University at New Orleans, New Orleans, Louisiana 70126, USA*
[12]*Tohoku University, Sendai, 980-8577 Japan*
[13]*University of Minnesota, Minneapolis, Minnesota 55455, USA*
[14]*Florida International University, Miami, Florida 33199, USA*
[15]*Ohio University, Athens, Ohio 45701, USA*
[16]*The George Washington University, Washington DC 20052, USA*
[17]*University of Houston, Houston, Texas 77204, USA*
[18]*Northwestern University, Evanston, Illinois 60201, USA*
[19]*Duke University and Triangle Universities Nuclear Laboratory, Durham, North Carolina 27708, USA*
[20]*University of Virginia, Charlottesville, Virginia 22901, USA*

(Received 14 August 2007; published 29 November 2207)

Kaon electroproduction from light nuclei and hydrogen, using ^{1}H, ^{2}H, ^{3}He, ^{4}He, and carbon targets has been measured at the Thomas Jefferson National Accelerator Facility. The quasifree angular distributions of Λ and Σ hyperons were determined at $Q^2 = 0.35$ (GeV/c)^2 and $W = 1.91$ GeV. Electroproduction on hydrogen was measured at the same kinematics for reference.

DOI: 10.1103/PhysRevC.76.054004 PACS number(s): 21.45.+v, 21.80.+a, 25.30.Rw, 27.10.+h

I. INTRODUCTION

Flavor degrees of freedom provide an invaluable tool for understanding hadron structure. Electromagnetic production of strangeness uses the well-understood photon as a probe of a nucleon or nuclear target, thereby creating an $s\bar{s}$ quark pair which is not part of the valence structure of the target. Thus electromagnetically induced strangeness is believed to influence the reaction dynamics such that a better understanding of the underlying dynamics of hadrons emerges.

Strangeness electro- and photoproduction on nuclei has the potential to deliver information on the hyperon-nucleon interaction in the nuclear medium, as well as on the final state interaction between nucleons and strange particles and the creation of coherent, bound hypernuclear states.

A comprehensive study of kaon electroproduction on light nuclei has been conducted in Hall C of the Thomas Jefferson National Accelerator Facility (Jefferson Lab or JLab). Data were obtained using electron beams of 3.245 GeV impinging on special high density cryogenic targets of ^{1,2}H and ^{3,4}He, as well as on a solid carbon target.

Comparing photo- and electroproduction, the main difference is that for photoproduction, we are at one kinematic point, $Q^2 = 0$, i.e., the photon is real. For electroproduction, $Q^2 \neq 0$, i.e., the kinematics moves away from the photon point. Because energy as well as three-momentum of the photon can be varied independently, virtual photons may probe the structure (form factors) of the hadrons involved in the reaction.

Until recently, the data base of cross sections of electro- and photoproduction of strangeness was sparse. In the case of photoproduction, considerable amounts of new high quality data for the proton have been published from experiments at JLab, the Electron Stretcher and Accelerator (ELSA), Physics Institute, Bonn University, Germany, the super photon ring-8 GeV (SPring-8) facility in Japan, the Grenoble Anneau Accelerateur Laser (GRAAL) in France, and the Laboratory

*F.Dohrmann@fzd.de

 ©2007 The American Physical Society

of Nuclear Science (LNS) at Tohoku University, Sendai, Japan (cf. Ref. [1] for a list of references). These data include cross sections, polarization asymmetries, tensor polarizations, and decay angle distributions. However, the data base for photoproduction on nuclei and thus implicitly the neutron remains sparse (cf. Refs. [2,3]). Only a few older measurements have been reported on deuterium [4,5] and carbon [6] targets.

Traditionally, ^{2}H and ^{3}He targets have been considered to be a good approximation for a free neutron target. In the present work, as in the majority of kaon electroproduction experiments, a positive kaon is detected in coincidence with the scattered electron. On the proton, this leads to two possible final states with either a Λ or Σ^0 hyperon, which are easily separable by a missing mass analysis. On the neutron, a Σ^- is produced as the final state. Due to the small mass difference of Σ^- and Σ^0 of 4.8 MeV/c^2 and the initial nucleon momentum distribution, the Σ contributions from the proton and neutron cannot be separated by missing mass. With increasing target mass, the separation between Λ and Σ distributions also gets worse because of the increasing Fermi momentum. Thus, ^{2}H and ^{3}He targets offer the best access to the neutron cross sections. Since a missing mass analysis, strictly speaking, can only determine the total Σ strength, the different N/Z ratio for the ^{2}H and ^{3}He targets should assist in further disentangling the Σ^0 and Σ^- contributions.

Systematic studies of heavier nuclei will then provide possibilities of investigating in-medium modifications of the elementary kaon electroproduction mechanism as well as the propagation of the outgoing K^+; e.g., experimental data on ^{12}C [6–9] show an effective proton number that disagrees with theoretical calculations [10], thereby indicating the need for modifications.

We present here the results of an experiment on the electroproduction of open strangeness on light nuclei with $A =$ 2, 3, 4, 12, which was performed in Hall C at Jefferson Lab. Also measured was the production on a hydrogen target. This facilitates direct comparison with the elementary $p(e, e'K^+)$ reaction for identical kinematics. Results of this experiment on the production of Λ hypernuclear states, $^3_\Lambda$H and $^4_\Lambda$H, have been presented in Ref. [11]. In this paper, we present the cross sections for the quasifree production of Λ, Σ^0, and Σ^-. To the best of our knowledge, this is the first reported kaon electroproduction measurement on helium isotopes.

II. EXPERIMENT

Experiment E91-016 had two runs, one that only used hydrogen and deuterium targets, and a subsequent one that also included helium and carbon targets. We present cross sections from the second run, which included data for all four few-body nuclei. Data were obtained using electron beams of 3.245 GeV impinging on special high density cryogenic targets of ^{1,2}H and ^{3,4}He. The target thicknesses were 289 mg/cm^2 for ^{1}H at 19 K, 668 mg/cm^2 for ^{2}H at 22 K, 310 mg/cm^2 for ^{3}He at 5.5 K, and 546 mg/cm^2 for ^{4}He at 5.5 K. The target lengths were approximately 4 cm for each target. In addition, data was taken on a 227 mg/cm^2 carbon target.

The scattered electrons were detected in the high momentum spectrometer (HMS, momentum acceptance $\Delta p/p \approx \pm 10\%$, solid angle $\approx$6.7 msr) in coincidence with the electroproduced kaons, detected in the short orbit spectrometer (SOS, momentum acceptance $\Delta p/p \approx \pm 20\%$, solid angle $\approx$7.5 msr). The detectors and coincidence methods have been described in detail for similar experiments in Hall C [12–14]. The detector packages of the two spectrometers are very similar, and a sketch of the setup of the experiment is shown in Fig. 1. Two drift chambers near the focal plane, used

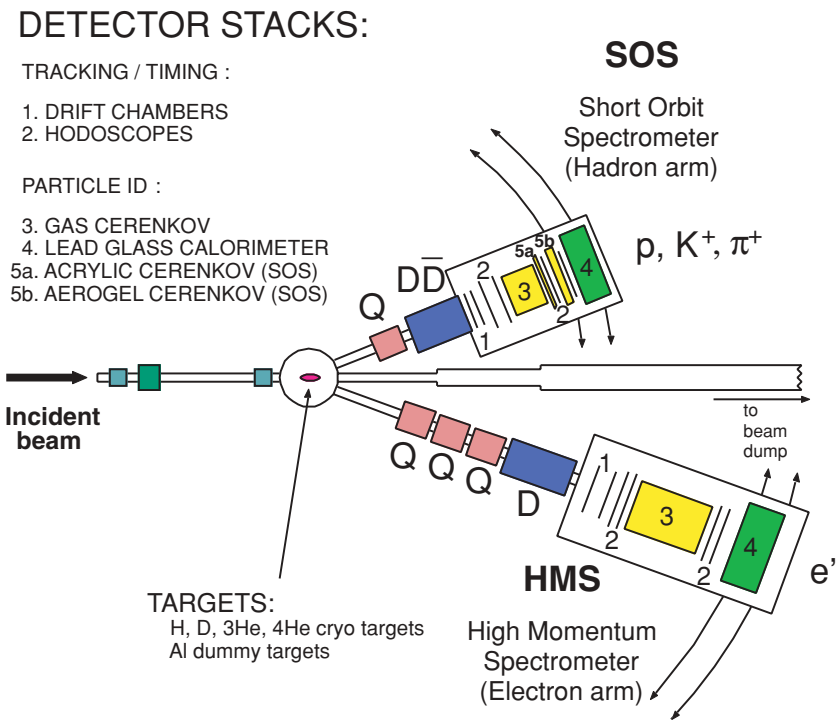

FIG. 1. (Color online) Setup of the experiment (modified from Refs. [12,15]). While the general setup was similar to other Hall C experiments, in this experiment an additional acrylic Čerenkov detector was used for better K^+/p discrimination.

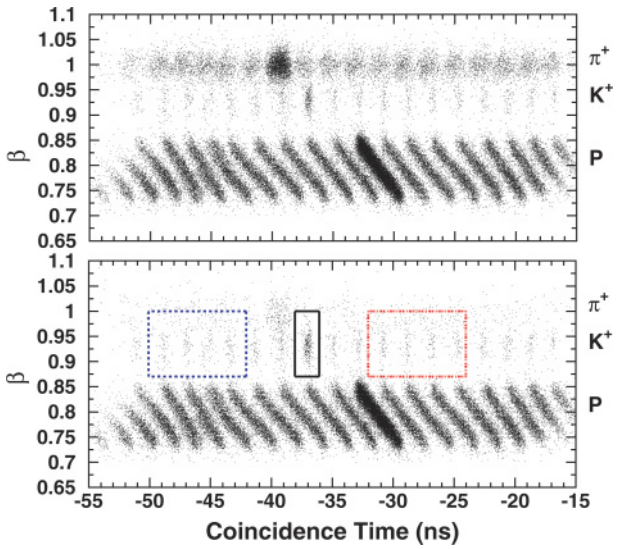

FIG. 2. (Color online) Real and random events of β vs the path-length-corrected coincidence time measured by the SOS spectrometer. Visible bands correspond to protons (low velocities), kaons and pions (high velocities). The tilt of the pion and proton bands reflects that the velocity was calculated assuming the particle was a kaon. The effect of particle identification (PID) cuts is shown in the bottom figure, where the fast pions were almost totally removed. The random events are determined by averaging over a number of random coincidence peaks as indicated by the blue dashed box and the red dot-dashed box. These are to be subtracted from the small box around the main coincidence peak. (An earlier version of this figure is shown in Ref. [16]).

for reconstructing the particle trajectories, are followed by two pairs of segmented plastic scintillators that provide the main trigger signal as well as the time-of-flight information. The time-of-flight resolution is ∼150 ps (σ). For electron identification, a lead-glass shower detector array together with a gas threshold Čerenkov is used to distinguish between e^- and π^-. For kaon identification in the SOS, a silica aerogel detector ($n = 1.034$) provides K^+/π^+ discrimination, while an acrylic Čerenkov counter ($n = 1.49$) is used for K^+/p discrimination.

Electroproduction processes involve the exchange of a virtual photon γ^* between projectile and target. The spectrometer setting for electron detection was kept fixed at an angle of 14.93° during the experiment, thereby holding the virtual photon flux constant (cf. Ref. [16]). The initial spectrometer angle of the kaon arm was 13.40°. This angle was varied to measure angular distributions with respect to the direction of γ^*. For γ^*, the invariant mass was $Q^2 = 0.35$ (GeV/c)^2, the virtual photon momentum was $|\vec{q}| = 1.77$ GeV/c, and the total energy in the photon-nucleon system was $W = 1.91$ GeV. Electroproduction on light nuclei was studied for three different angle settings with respect to the initial kaon angle, 13.40°. The corresponding angles between the virtual photon γ^* and the ejected kaon K are $\theta^{\rm lab}_{\gamma^* K^+} \simeq 1.7°, 6°, 12°$. These correspond to increasing the momentum transfer to the hyperon [$|\,t\,| \simeq (0.12,\ 0.14,\ 0.23)$ GeV^2]. The central spectrometer momenta were 1.29 GeV/c for the kaon arm and 1.57 GeV/c for the electron arm.

III. DATA ANALYSIS

The essential element of the data analysis for the present work is a clear identification of scattered electrons coincident with kaons against a large background of pions and protons. Figure 2 shows the measured hadron velocity in the SOS vs the coincidence time between the two spectrometers. The latter has been projected back to the target by using the kaon mass as default. It thus represents the proper coincidence time only for kaons, the particles of interest. Clearly visible is the 2-ns RF time structure of the beam. The top panel shows the distributions before and the bottom panel after applying an analysis cut on the aerogel Čerenkov detector. In-time (e, K^+) coincidences are selected by a cut on β and coincidence time. Real (e, π) coincidences are visible about 2 ns below the kaon peak, whereas real (e, p) coincidences appear at about 6 ns above the kaon peak. The background from uncorrelated (e, K^+) pairs was subtracted using distributions from out-of-time coincidences, a standard procedure for Jefferson Lab Hall C experiments [13,15]. Defining the out-of-time window such that it does not include any in-time coincidences of (e, π) and (e, p), this procedure also corrects for any remaining pion and proton background in the in-time kaon window. The contamination of the kaon sample after the aerogel cut is on the order of 2–4%. After subtracting random coincidences, cf. Fig. 2, the kaon sample is very clean with a contamination well below 1%. The efficiency for kaon identification is 82%.

Following Refs. [17,18], the notation of strangeness electroproduction may be introduced by

$$p(p^\mu) + e\left(q_e^\mu\right) \rightarrow e'\left(q_{e'}^\mu\right) + K\left(p_K^\mu\right) + Y\left(p_Y^\mu\right), \qquad (1)$$

with the four-momenta $q_e^\mu = (E_e, \vec{q}_e), q_{e'}^\mu = (E_{e'}, \vec{q}_{e'})$ of the incoming and outgoing electron, $q^\mu = (\omega, \vec{q})$ of the virtual photon, $p_p^\mu = (E_p, -\vec{q}), p_K^\mu = (E_K, \vec{p}_K)$, and $p_Y^\mu = (E_Y, -\vec{p}_K)$. The virtual photon is defined by the difference of the four-vectors of the incoming and outgoing electron, $q^\mu = q_e^\mu - q_{e'}^\mu$. The kinematics are shown in Fig. 3, where the lepton and hadron planes are defined. The virtual photon connects both planes kinematically.

After proper electron and kaon identification, the measured momenta (magnitude and direction with respect to the incoming beam) allow for a full reconstruction of the missing energy and missing momentum of the recoiling system.

The missing energy and missing momentum of the recoiling nucleons are calculated, *viz*.,

$$E_X = E_e - E_{e'} + M_{\rm targ} - E_K = \omega + M_{\rm targ} - E_K, \qquad (2)$$

$$\vec{P}_X = \vec{q} - \vec{p}_K, \qquad (3)$$

where $M_X = \sqrt{(E_X^2 - |\vec{P}_X|^2)}$ is the missing mass, and $M_{\rm targ}$ denotes the target mass. The four-momentum transfer to the nucleons is given by the Mandelstam variable t,

$$t = \left(q^\mu - p_K^\mu\right)^2 = (\omega - E_K)^2 - |\vec{q}|^2 - |\vec{P}_K|^2 + 2|\vec{q}||\vec{P}_K|\cos\theta_{pK}. \qquad (4)$$

Final states of the $A(e, e'K)X$ reaction for $A = 1, 2, 3, 4, 12$ are visible in Fig. 4. The missing mass M_X is calculated from the four-momenta q^μ of the virtual photon and the

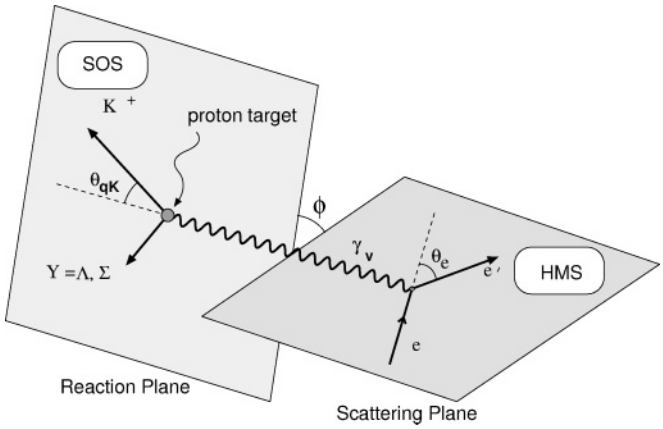

FIG. 3. Kinematics of kaon electroproduction: the reaction (hadron) and scattering (lepton) planes are connected by the virtual photon which lies in both planes. The electron scattering angle is denoted by θ_e, the kaon scattering angle between the kaon and the direction of the virtual photon is denoted by $\theta_{\gamma K}$. Typically for electroproduction experiments in Hall C of JLab, the ejected K^+ is detected by the SOS spectrometer in coincidence with the scattered e' detected by the HMS spectrometer (from Ref. [12]).

four-momentum p_K^μ of the detected kaon, *viz.*,

$$M_X^2 = \left(q^\mu + P_{\text{targ}}^\mu - p_K^\mu\right)^2, \tag{5}$$

where $P_{\text{targ}}^\mu = (M_{\text{targ}}, 0, 0, 0)$ is the target four-momentum.

Missing mass distributions have been created for the in-time (e, K) coincidences as well as a sample of the out-of-time coincidences; the latter then were subtracted with the appropriate weight. For the cryogenic targets, the background from the target cell walls was determined by a measurement from an empty cell replica. Data from this replica were subjected to the same analysis. As an example, for ^{3}He, Fig. 5 shows the typical sizes of the various background contributions compared to the raw data. Background contributions are subtracted from the raw distribution in the following way: $M_X = M_{\text{real}} - M_{\text{random}} - (M_{\text{real}}^{\text{cell}} - M_{\text{random}}^{\text{cell}})$.

Figure 4 shows background-subtracted missing mass distributions for all four targets. For the hydrogen target, the missing mass distributions allow for an unambiguous identification of the electroproduced hyperon, either a Λ or a Σ^0. The well-known masses of these two hyperons also serve as an absolute mass calibration with an accuracy of better than 2 MeV.

On the deuterium target, the two distributions are significantly broadened because of the presence of a nucleon spectator and the Fermi motion of the target nucleons. Furthermore, the Σ distribution now is comprised of two possible final states, either a $\Sigma^0 n$ or a $\Sigma^- p$, the latter from the reaction with a neutron inside the target. Since the mass difference between Σ^0 and Σ^- is small compared to the width of the distributions, these two final states are completely unresolved. In Fig. 4 it is also obvious that the radiative tail from the Λ distribution contributes significantly to the strength observed in the Σ mass region. For increasing A, the peaks associated with Λ and Σ hyperons further broaden. Whereas

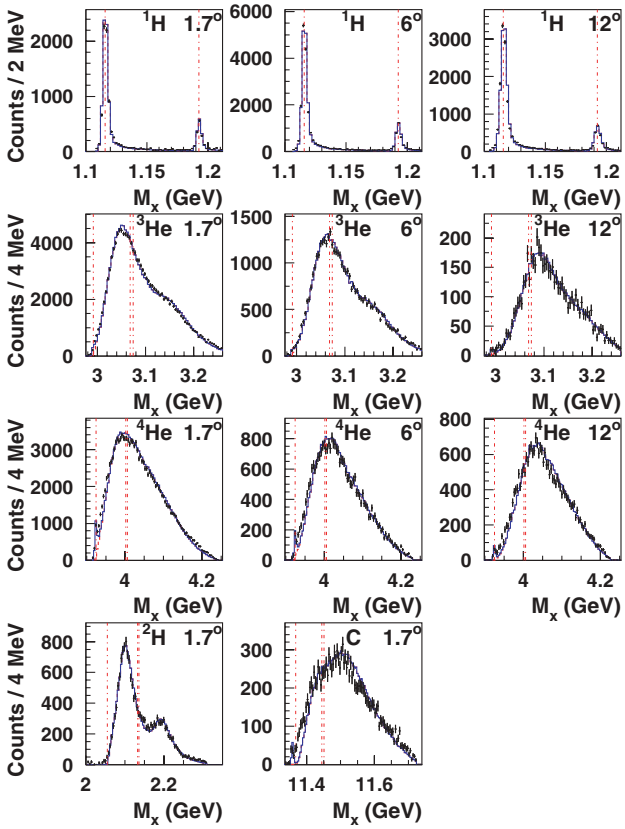

FIG. 4. (Color online) Reconstructed missing mass spectra for all five targets at all kinematic settings as indicated. For ^{1}H, ^{3}He, and ^{4}He, three kinematic settings were measured; for ^{2}H and C targets, only one kinematic setting (1.7°) was measured. The blue line represents the respective fit to each spectrum. Vertical dot-dashed lines show the (lowest) thresholds for the Λ and $\Sigma^{0,-}$ production for the various targets. For hydrogen, these lines correspond to the pole masses of the Λ and Σ^0 hyperons, respectively.

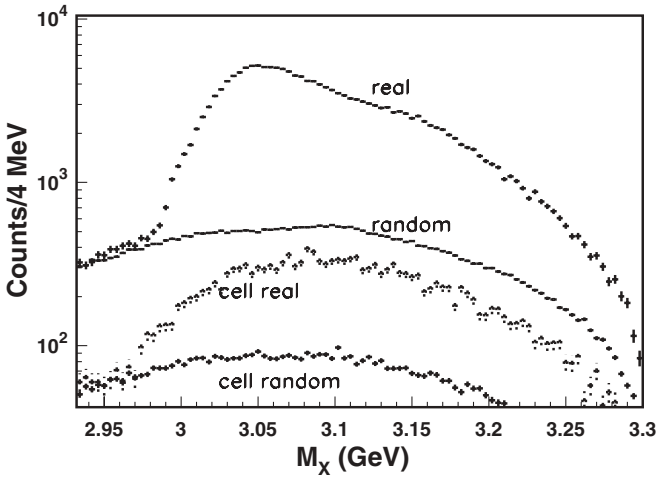

FIG. 5. Raw missing mass spectra for the ^{3}He target. From top to bottom the contributions of real events, random background events, as well as the background contributions of the target cell are shown.

for ^{3}He a small shoulder associated with Σ is still visible, only an indistinct broad distribution remains for the ^{4}He target.

This challenges any extraction of the underlying three reaction channels $\gamma^* + p \to \Lambda + K^+$, $\gamma^* + p \to \Sigma^0 + K^+$, and $\gamma^* + n \to \Sigma^- + K^+$. The following section will describe an attempt to disentangle the three reaction channels by means of a Monte Carlo simulation that models the spectrometer acceptances as well as the reaction mechanism.

The electroproduction cross section may be written as

$$\frac{d^5\sigma}{dE_{e'}d\Omega_{e'}d\Omega_K} = \Gamma\frac{d^2\sigma}{d\Omega_K}, \tag{6}$$

where Γ denotes the virtual photon flux factor

$$\Gamma = \frac{\alpha}{2\pi^2}\frac{E_{e'}}{E_e}\frac{1}{Q^2}\frac{W^2-M^2}{M}\frac{1}{1-\varepsilon}, \tag{7}$$

where α is the fine structure constant, and ε is the longitudinal polarization of the virtual photon,

$$\varepsilon = \left(1 + 2\frac{|\vec{q}|^2}{Q^2}\tan^2(\theta_e/2)\right)^{-1}. \tag{8}$$

The total energy in the virtual-photon–target center of mass is given by $W^2 = s = (q^\mu + p^\mu_{\text{target}})^2$ and can be expressed in the laboratory reference frame by $W^2 = M^2 + 2M\omega - Q^2$. To facilitate comparison with the scattering on the proton, both for calculating W as well as in Eq. (7), M is taken to be the nucleon mass for all targets discussed here.

The ^{1}H$(e, e'K^+)X$ data were used to provide consistent normalization data as well as to test available isobar models and to develop a global model that would describe the data. While reasonable agreement was found with the Saclay-Lyon model [19], the best description of the data within the kinematic range of this experiment was achieved by a dedicated simple model. This model had already been developed for the first experimental run on $A = 1, 2$ targets [20]. Unlike the Saclay-Lyon model, it is not based on separated response functions. Instead, the unpolarized twofold center of mass cross section is modeled and taken as input for the simulations, which then provides a fivefold laboratory cross section as output.

The model describes the unpolarized differential cross section for ^{1}H$(e, e'K^+)\Lambda$ by a factorization ansatz of four kinematic variables:

$$\left.\frac{d^2\sigma}{d\Omega}\right|_\Lambda (Q^2, W, t, \phi) = f(Q^2) \times N \cdot g(W)h(t)i(\phi), \tag{9}$$

with a normalization constant $N = 5.4724$ and the four functions

$$f(Q^2) = \text{constant} = c_1^f, \tag{10}$$

$$g(W) = c_1^g\frac{P_K^{\text{cm}}}{(W^2-M_p^2)W} + c_2^g\frac{W^2}{c_3^g W^2 + (W^2-1.72^2)^2}, \tag{11}$$

$$h(t_{\min}-t) = \exp\left(c_1^h(t_{\min}-t)\right), \tag{12}$$

$$i(\phi) = c_1^i + c_2^i\cos(\phi) + c_3^i\cos(2\phi). \tag{13}$$

TABLE I. Fit parameters for the model cross section for ^{1}H$(e, e'K^+)\Lambda$ from Ref. [20].

	c_1	c_2	c_3
$f(Q^2)$	0.430 μb/sr		
$g(W)$	4.470 MeV^2	0.00089 MeV^2	0.0062 MeV^2
$h(\Delta t)$	−2.14		
$i(\phi)$	0.438	−0.048	0.008

The $c_{1,2,3}^{f,g,h,i}$ are parameters which were determined through a fit to the data taken during the first experimental run [20,21]. These parameters are given in Table I.

The functional form of the t dependence in Eq. (12) has been taken from an earlier work by Brauel *et al.* [22], while the ϕ dependence was studied during the first run of the experiment [20]. Equation (11) shows that the dependence on the total photon energy W is composed of a phase space factor and a Breit-Wigner resonance. The observed Q^2 dependence is very weak, and it is set to a constant.

For the electroproduction of Σ^0 hyperons, ^{1}H$(e, e'K^+)\Sigma^0$, only a single, energy-dependent phase space factor is used. Following [23] we obtain

$$\left.\frac{d^2\sigma}{d\Omega}\right|_\Sigma (W) = c_1\frac{P_K^{\text{c.m.}}}{(W^2-M_p^2)W}c_1 = 1.32\,\text{GeV}^2\mu\text{b/sr}, \tag{14}$$

where the constant c_1 was determined by Koltenuk [24].

Unlike hydrogen, the missing mass distributions for deuterium and the other nuclear targets do not show two clearly separable peaks, cf. Fig. 4, as discussed above. To extract information on the quasifree Σ^0 as well as Σ^- production, one has to rely on assumptions about the nuclear dependence of the Σ^0. In this analysis, we determine the ratio of Λ to Σ production for hydrogen and then keep this ratio fixed in the proton model that enters into the simulation for the nuclear cross section. Nuclear effects thus contribute to the systematic uncertainties (cf. Refs. [2,25]). If such an assumption is not made, only a combined Σ contribution may be deduced, as in Refs. [5,26].

The data shown in Fig. 4 were compared with a dedicated Monte Carlo simulation that modeled the spectrometer optics and acceptance, kaon decay, small angle scattering, energy loss, and radiative corrections [12,27]. The process of extracting the respective cross sections described in detail in Refs. [13,15] relies upon a ratio of the measured yield from experiment, Y_{exp}, normalized to a simulated yield from the above-mentioned Monte Carlo simulation, Y_{MC}, which is used as a scale factor for the model cross section used in the Monte Carlo, *viz.*,

$$\frac{d^2\sigma}{d\Omega} = \frac{Y_{\text{exp}}}{Y_{\text{MC}}}\left.\frac{d^2\sigma}{d\Omega}\right|_{\text{model}}. \tag{15}$$

This approach is also known as the method of correction factors, cf. Ref. [28]. For $A = 2, 3, 4, 12$, the $A(e, e'K^+)X$ process was modeled as quasifree scattering on target nucleons inside the target. Since to the best of our knowledge, no dedicated models are available for the electroproduction on these nuclei, the elementary cross section models in

Eqs. (9)–(13) for Λ and Eq. (14) for Σ are used. The respective cross sections are multiplied by the number of protons Z or neutrons N. Since no separate model for production on the neutron is available, we use the model (14) for both Σ^0 and Σ^-. The model is convolved with spectral functions [29] for the respective target nucleus.

The spectral functions provide the four-momenta of the target nucleons inside the target. For the $A = 2$ case, deuteron momentum distributions taken from either the Bonn potential [30] or the Av18 potential [31] gave essentially identical results. Obviously neither of these models incorporate any possible in-medium behavior of the nucleons inside the target nor final state interaction, as will be discussed below. For the nuclear targets, final state interactions in the vicinity of the respective quasifree thresholds are taken into account using an effective range approximation [32].

The final state interaction of the hyperon with the remaining target nucleon has to be taken into account, whereas the kaon nucleon final state interaction is small; the ΛN total cross section is more than two orders of magnitude larger than the K^+N total cross section.[1] We use an effective range approximation (ERA), by which the modeled cross section is modified by an enhancement factor I (cf. Watson and Migdal [33,34]), that is,

$$\sigma_K^{YN\,\mathrm{FSI}} = I\sigma_K = \frac{1}{|J_l(k_{\mathrm{rel}})|^2}\sigma_K, \tag{16}$$

in terms of the complex Jost function J_l for the lth partial wave. k_{rel} is the relative momentum between the hyperon and the nucleon (see also Chapters 12 and 14 of Ref. [35]). A hyperon-nucleon (YN) potential V is used to describe the final state interaction, for which only the s-wave part is taken into account. The s-wave Jost function may then be written as

$$J(k_{\mathrm{rel}}) = \frac{k_{\mathrm{rel}} - i\beta}{k_{\mathrm{rel}} - i\alpha}, \tag{17}$$

where α and β are determined from the scattering length a and effective range r_e of the hyperon-nucleon potential, *viz.*,

$$\tfrac{1}{2}r_e(\alpha - \beta) = 1, \quad \tfrac{1}{2}r_e\alpha\beta = -\tfrac{1}{a}. \tag{18}$$

In this ansatz, there are no free parameters; the magnitude of the enhancement factor is fully determined by the effective range r_e and the corresponding scattering length a, both being parameters of the hyperon-nucleon potential chosen. For the $A = 2$ targets, the full Jost function ansatz gave a less satisfactory description of the data than for the helium targets. An even simpler approach for an ERA, studied in Ref. [20] and following a prescription described in Ref. [36], was used. The s-wave phase shift δ_0 is calculated via the Bethe formula, and the enhancement factor is given by

$$k_{\mathrm{rel}}\cot\delta_0 = -\frac{1}{a} + 0.5r_e k_{\mathrm{rel}}^2, \quad I = \left(\frac{\sin(\delta_0 + k_{\mathrm{rel}}r)}{\sin k_{\mathrm{rel}}r}\right)^2. \tag{19}$$

For the helium targets, however, the full Jost function ansatz gave much better results. For the data sets presented in this paper, we use the Nijmegen 97f YN potential [37], with scattering lengths a taken from Ref. [37] and effective ranges of r_e taken from the Nijmegen 89 [38], since Ref. [37] does not provide these parameters. In all cases and for every hyperon-nucleon potential tested, the singlet values for a and r_e gave more satisfactory results than triplet values. For the Σ hyperons, the Nijmegen 97f and the Jülich A also provide a and r_e for the ΣN interaction. Using these values, an enhancement factor due to the ΣN final state interaction was introduced. However, the fits to the data were more strongly influenced by the ΛN final state interaction. In Fig. 6, we show the effect of applying the final state interaction in an ERA to our model in the low-mass Λ region.

TABLE II. Final state interaction enhancement factors. The factor is the ratio of the integrated yield of missing mass spectra before ($Y_{\mathrm{no\_FSI}}$) and after (Y_{FSI}) applying the final state contribution for the respective kinematic setting and target. The integration is carried out over the kinematic range for the respective targets, cf. Figs. 4 and 7.

Target	Angle (deg)	$Y_{\mathrm{FSI}}/Y_{\mathrm{no\_FSI}}$		
		Λ	Σ^0	Σ^-
^{2}H	1.7	4%	3%	2%
^{3}He	1.7	15%	8%	10%
^{3}He	6	12%	7%	9%
^{3}He	12	9%	5%	7%
^{4}He	1.7	13%	7%	11%
^{4}He	6	12%	6%	9%
^{4}He	12	7%	4%	10%
^{12}C	1.7	10%	5%	8%

In Table II, we show the influence of the FSI on the simulated missing mass yields. The simulated missing mass is weighted by the respective model cross section. If the cross section is multiplied by an enhancement factor, the missing mass spectra are influenced. Table II gives the ratio of the integrated yields $Y_{\mathrm{FSI}}/Y_{\mathrm{no\_FSI}}$ for missing mass distributions (cf. Figs. 4 and 7) with or without FSI for the model (9) discussed above. Choosing a different cross section model would change these values only by 1%–3%. Also, different final state interaction models (e.g., Nijmegen 97f, Jülich A) do not change the yield ratio by more than 3%.

For the helium-3 and helium-4 target nuclei (and also for carbon), the analysis was performed analogously to the $A = 2$ case. However, the electroproduction of strangeness on helium targets (and on carbon, though with rather poor statistics) triggers two investigations: the quasifree production of open strangeness on the light nuclear target as well as the production of bound hypernuclear states. The missing mass distributions for these targets are shown in Figs. 4 and 7. It is obvious from both figures that the investigation of the quasifree reactions on the one hand and structures near the respective thresholds for quasifree production on the other hand do not completely decouple because of the limited mass resolution of the missing mass distributions. Therefore the quasifree distribution and the coherent distribution overlap.

[1] http://pdg.lbl.gov/2006/hadronic-xsections/hadron.html.

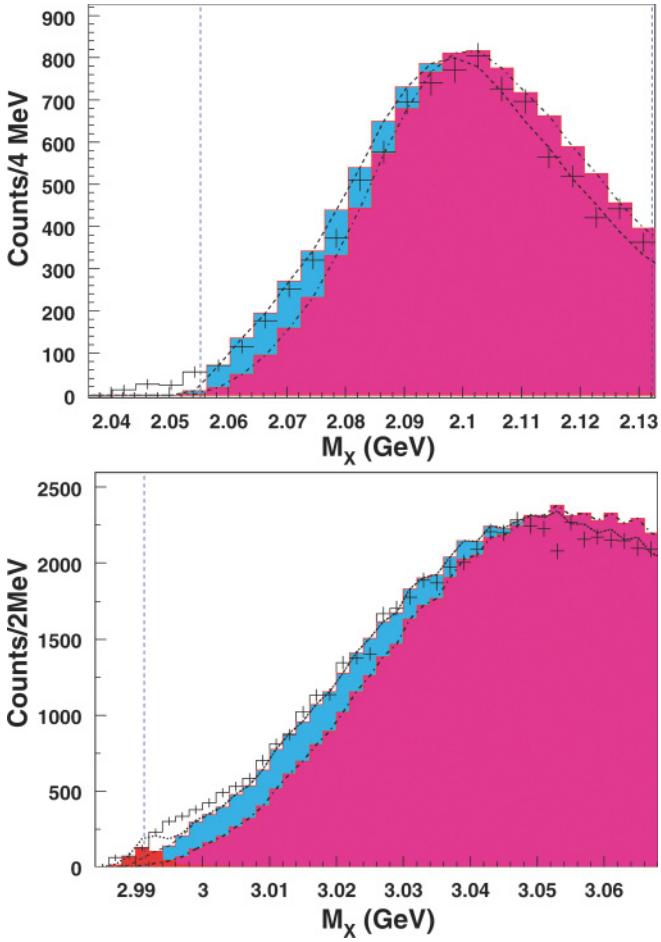

FIG. 6. (Color online) Effects of including FSI for the fits to the data on ^{2}H (upper panel) and ^{3}He (lower panel) in the low-mass Λ region. The fitted Λ contribution without FSI is given by the dark color, dash-dotted line. Λ contributions including FSI are given by the light-blue, dashed line. For ^{3}He, the $^3_\Lambda$H bound state is shown in red. The total fit (sum of all contributions) is given by the dotted line. Vertical dot-dashed lines are as in Fig. 4.

The following describes the extraction of the cross section. For the ^{1}H$(e, e'K^+)$ data, we fit the missing mass spectra M^{data} with the ansatz

$$M^{\text{data}}(\text{H}) = f_{\text{H},\Lambda} M_\Lambda^{\text{model}}(\text{H}) + f_{\text{H},\Sigma^0} M_{\Sigma^0}^{\text{model}}(\text{H}), \qquad (20)$$

with two free fit parameters $f_{\text{H},\Lambda}$ and f_{H,Σ^0} for the simulated missing mass distributions $M_{\Lambda,\Sigma^0}^{\text{model}}$. Once these two parameters are obtained, the cross section in the laboratory may be obtained by evaluating the model cross section for the simulation at the specific kinematic conditions of the experiment, as stated above. These two model cross sections are then multiplied by the respective fit parameters obtained in Eq. (20). Moreover, we define the important ratio of the fit parameters

$$R_{\Lambda\Sigma^0} = \frac{f_{\text{H},\Lambda}}{f_{\text{H},\Sigma^0}}. \qquad (21)$$

For targets with $A \geqslant 2$, Eq. (20) has to be modified to incorporate the possible conversion of a target neutron into a Σ^- hyperon as follows:

$$M^{\text{data}}(A) = f_{A,\Lambda} M_\Lambda^{\text{model}}(A) + f_{A,\Sigma^0} M_{\Sigma^0}^{\text{model}}(A) + f_{A,\Sigma^-} M_{\Sigma^-}^{\text{model}}(A). \qquad (22)$$

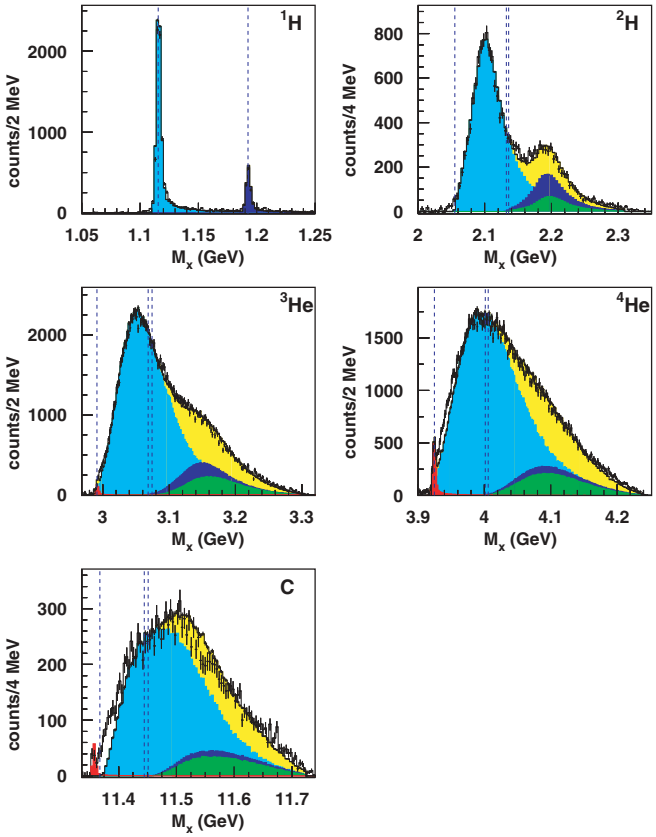

FIG. 7. (Color online) Reconstructed missing mass spectra for six targets at one kinematic setting ($\langle 1.7^\circ \rangle$). Simulated quasifree reactions A$(e, e'K^+)Y$ are indicated by colors: $Y = \Lambda$ (light blue), $Y = \Sigma^0$ (blue), $Y = \Sigma^-$ (green), bound states $^3_\Lambda$H, $^4_\Lambda$H, $^{12}_\Lambda$B (red), and sum of all simulated contributions (yellow). Vertical dot-dashed lines are as in Fig. 4.

Here the simulated missing mass distributions $M_Y^{\text{model}}(A)$, $Y = \Lambda$, Σ^0, Σ^- include both the respective model cross section and the respective enhancement factors $I_Y(A)$ due to the final state interaction. The respective cross sections are given by

$$\sigma_Y(A) = f_{A,Y} I_Y(A) \sigma_Y^{\text{model}}(A). \qquad (23)$$

In the following, if not explicitly stated otherwise, it is assumed that the model cross section $\sigma_Y^{\text{model}}(A)$ themselves do not include the final state interaction. Enhancements of the model cross sections due to the final state interaction are described by enhancement factors $I_Y(A)$.

Equation (22) poses a fitting problem with three free fit parameters $f_Y(A)$ for which this experiment is not able to distinguish directly the contributions of either Σ hyperon. Thus for targets with $A \geqslant 2$, it is assumed that this ratio (21) is the same for the bound protons in the respective nucleus, i.e.,

$$R_{\Lambda\Sigma^0} = \frac{f_{\text{H},\Lambda}}{f_{\text{H},\Sigma^0}} = \frac{f_{\text{A},\Lambda}}{f_{\text{A},\Sigma^0}}, \quad f_{A,\Sigma^0} = \frac{f_{A,\Lambda}}{R_{\Lambda\Sigma_0}(\text{H})}. \qquad (24)$$

TABLE III. Differential cross sections for electroproduction of $K^+\Lambda$, $K^+\Sigma^{0,-}$ final states on $A = 1, 2, 3, 4, 12$ targets. A prescription for separating the Σ^0, Σ^- cross sections is discussed in the text. Independently, a combined $K^+\Sigma$ cross section is given. $\sigma_{\rm lab}$ denotes the fivefold laboratory differential cross section $d^5\sigma/d\Omega_e\, dE_e\, d\Omega_K$ (in nb/GeV sr^2). $\sigma_{\rm c.m.}$ denotes the twofold differential cross section $d^2\sigma/d\Omega$ (in μb/sr) in the virtual-photon–nucleus center of mass system. Uncertainties given include the combined statistical and fitting uncertainties. Uncertainties from Table IV have to be added to these values. The first row shows data for 1.7° averaged over the azimuth. A 9% systematic error has to be added to the cross sections given, see text and Table IV. Note that values are not given per contributing nucleon, cf. text.

Target	^{1}H		^{2}H		^{3}He		^{4}He		^{12}C	
$\theta^{\rm lab}_{\gamma^*,K^+}$(°)	$\sigma_{\rm lab}$	$\sigma_{\rm cm}$	$\sigma_{\rm lab}$	$\sigma_{\rm cm}$	$\sigma_{\rm lab}$	$\sigma_{\rm cm}$	$\sigma_{\rm lab}$	$\sigma_{\rm cm}$	$\sigma_{\rm lab}$	$\sigma_{\rm cm}$
					Λ					
⟨1.7⟩	10.6 ± 0.2	0.47 ± 0.01	9.4 ± 0.2	0.41 ± 0.01	21.7 ± 0.2	0.95 ± 0.01	19.8 ± 0.2	0.86 ± 0.01	61.6 ± 1.5	2.64 ± 0.07
1.7	9.8 ± 0.4	0.43 ± 0.03	9.4 ± 0.5	0.41 ± 0.02	20.4 ± 0.3	0.89 ± 0.02	18.2 ± 0.3	0.79 ± 0.02		
6	9.9 ± 0.1	0.44 ± 0.01			19.5 ± 0.3	0.87 ± 0.02	17.7 ± 0.3	0.79 ± 0.03		
12	7.6 ± 0.1	0.36 ± 0.01			15.0 ± 0.5	0.71 ± 0.04	14.2 ± 0.4	0.67 ± 0.02		
					Σ^0					
⟨1.7⟩	3.0 ± 0.2	0.12 ± 0.01	2.8 ± 0.2	0.11 ± 0.02	6.4 ± 0.2	0.25 ± 0.01	6.3 ± 0.1	0.25 ± 0.01	20.7 ± 0.5	0.81 ± 0.02
1.7	3.0 ± 0.4	0.12 ± 0.01	3.0 ± 0.2	0.12 ± 0.01	6.5 ± 0.2	0.26 ± 0.01	6.2 ± 0.2	0.25 ± 0.01		
6	3.3 ± 0.1	0.14 ± 0.01			6.8 ± 0.2	0.27 ± 0.01	6.6 ± 0.2	0.24 ± 0.01		
12	3.2 ± 0.1	0.14 ± 0.01			6.6 ± 0.2	0.29 ± 0.01	6.6 ± 0.2	0.29 ± 0.01		
					Σ^-					
⟨1.7⟩			1.9 ± 0.2	0.08 ± 0.01	4.6 ± 0.2	0.18 ± 0.01	4.8 ± 0.2	0.19 ± 0.01	16.5 ± 2.6	0.64 ± 0.1
1.7			1.8 ± 0.5	0.07 ± 0.02	3.9 ± 0.4	0.15 ± 0.02	4.6 ± 0.4	0.18 ± 0.02		
6					3.5 ± 0.5	0.14 ± 0.02	2.3 ± 0.6	0.09 ± 0.02		
12					3.3 ± 1.2	0.14 ± 0.05	0.3 ± 0.6	0.01 ± 0.02		
					Σ					
⟨1.7⟩			4.7 ± 0.2	0.19 ± 0.02	10.5 ± 0.2	0.42 ± 0.02	11.1 ± 0.3	0.44 ± 0.02	37.0 ± 2.6	1.45 ± 0.10
1.7			4.9 ± 0.6	0.19 ± 0.02	9.9 ± 0.4	0.39 ± 0.02	10.8 ± 0.5	0.43 ± 0.02		
6					9.7 ± 0.4	0.39 ± 0.02	9.0 ± 0.6	0.36 ± 0.02		
12					9.3 ± 0.9	0.40 ± 0.04	7.0 ± 0.2	0.30 ± 0.02		

Instead of fitting f_{A,Σ^0}, this parameter is calculated from the fitted $f_{A,\Lambda}$, using the results from the previous fit to the hydrogen data.

With f_{A,Σ^0} determined via Eq. (24), then Eq. (22) reduces to a fitting problem with only two free parameters.

For ^{3}He, ^{4}He, and ^{12}C, one additional parameter that refers to Λ bound states for the specific nuclear target has to be taken into account. For ^{4}He, a $^4_\Lambda$H bound state is clearly visible for all three kinematic settings just below the ^{3}H-Λ threshold of 3.925 MeV (cf. Figs. 4 and 7). For ^{3}He, just below the ^{2}H-Λ threshold of 2.993 MeV, the $^3_\Lambda$H bound state is barely visible as a weak shoulder for 1.7°, but it is clearly present for 6° and 12° (cf. Fig. 4). For carbon, the $^{12}_\Lambda$B bound state is clearly visible in the respective missing mass spectrum. The fits to the respective bound states for the helium targets and carbon do include one extra term for the bound state to be fitted. This extra term is not shown in Eq. (22); however, it contributes only over very narrow ranges of the fit and does not cause ambiguities in the procedure.

In the next section we focus on the extraction of the quasifree cross sections, angular distributions, and nuclear dependence for the respective targets.

IV. RESULTS AND DISCUSSION

The measurement presented in this work provides data for targets with $A = 1$–4 and carbon. The fivefold differential cross sections $d^5\sigma$ as well as the twofold center of mass differential cross section $d^2\sigma$ per nucleus are given in Table III. Unlike in our previous paper on hypernuclear bound states [11], these cross sections have not been normalized to the number of contributing nucleons n (e.g., ^{3}He: $n_\Lambda = n_{\Sigma^0} = 2$, $n_{\Sigma^-} = 1$; ^{4}He: $n_\Lambda = n_{\Sigma^0} = n_{\Sigma^-} = 2$).

We chose a binned maximum likelihood method (cf. Ref. [39]) for fitting the simulated distributions to the data. This procedure was already successfully used in another electroproduction experiment using the same equipment (cf. Ref. [15]). The fits were not constrained to fit the data only in specific regions of M_X. The binning of the respective missing mass distributions was chosen between 2 and 4 MeV and had no noticeable effect on the cross section extraction.

The angular distributions were restricted to a common range covered in azimuthal angle ($180° \pm 24°$). For the settings with near parallel kinematics, 1.7°, however, the full azimuth was accessible. The uncertainties given in Table III reflect statistical and fitting uncertainties. In the following, we discuss systematic uncertainties to be added to the uncertainties in Table III. These uncertainties are tabulated in Table IV. Correlated systematic uncertainties due to yield corrections, including efficiency corrections, dead times, and event losses, are ∼3%; while uncorrelated uncertainties, including time-of-flight determination (∼2%), particle identification (∼2%), absorption of kaons in the spectrometer and target material (∼3%), and kaon decay (∼3%), amount in total to ∼5%

TABLE IV. Breakdown of systematic uncertainties. These uncertainties have to be added to the uncertainties given in Table III.

Type	Uncertainty (%)
Experimental systematics	6%
Cross section model	6%
FSI model	3%
Total	9%

(cf. Ref. [40]), thereby yielding a combined uncertainty of ∼6% from these sources. Uncertainties due to the analysis approach will be discussed below.

For the extraction, separate M_X distributions were generated for quasifree production of Λ, Σ^0, and Σ^- hyperons, and the sum of these spectra was fitted to the total kaon M_X spectrum using a maximum likelihood fit. The fit parameters f_A and f_H [cf. Eqs. (20)–(24)] were roughly of order unity. For $A = 3$ and $A = 4$, bound state contributions for ${}^{3,4}_{\Lambda}$H, also included, were discussed in Ref. [11]. For carbon, however, the ${}^{12}_{\Lambda}$B bound state is bound so deeply that omitting it from the fits changes the respective cross sections by less than 0.3%. We estimate the laboratory cross section for the ${}^{12}_{\Lambda}$B to be on the order of $\sigma_{\rm lab} \sim (.9 \pm .2\,({\rm stat}))$ nb/GeV sr^2, $\sigma_{\rm c.m.} \sim (17.8 \pm 4.5\,({\rm stat}))$ nb/sr, where both cross sections have been divided by $n_p = 6$. We note, however, that we do not resolve ground or excited states of ${}^{12}_{\Lambda}$B, as were resolved in other experiments [8], such that our cross section estimate represents an integral value only.

The uncertainties of the cross section determination of Σ^0 are tied to those of Λ, since the ratio of Σ^0 to Λ production is fixed to the hydrogen results. However, any deviation from this assumption will result in large uncertainties on the Σ^- cross section extracted from nuclei.

Alternatively, we include a combined cross section for Σ^0 and Σ^-, the sum of the extracted cross sections for both Σ hyperons. We extracted the combined Σ cross section from a unconstrained fit of just two quasifree distributions for Λ and Σ to the respective data for all targets. For the combined Σ analysis, results agree with the main analysis within uncertainties ($\leqslant$3% for Λ, $\leqslant$ 10% for Σ).

Figures 8 and 9 display the cross sections for all three hyperons for ^{3,4}He in the center of mass system. For comparison, the quasifree distributions from hydrogen are displayed as open symbols. For convenience, the hydrogen values have been scaled by a factor of 2. In general, the distributions are similar and seem to be strongly imprinted by the underlying kinematics. While the angular distributions for the Λ hyperon drop with increasing $\theta_{\rm lab}$, the Σ^0 distributions stay nearly flat. This is also observed for ^{3}He and ^{4}He. Considerably different are the Σ^- distributions for the respective hyperons. For ^{3}He, the Σ^- angular distribution does not show any strong dependence on the angle, similar to the Σ^0 distribution. For ^{4}He, however, the Σ^- distribution drops significantly with angle. With increasing angle, the remaining strength seems to be exhausted by Λ and Σ^0 alone, so that the Σ^- cross section extracted for the ^{4}He at the largest angle is very small.

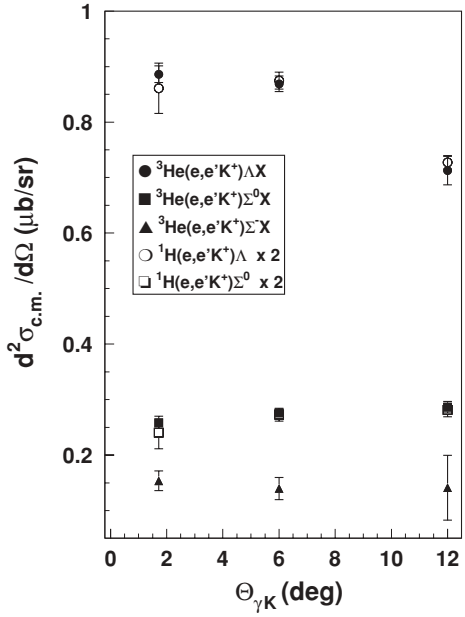

FIG. 8. Comparison of the nuclear cross section for quasifree Λ, Σ^0, and Σ^- production on ^{3}He targets. For comparison, the respective quasifree distributions on the proton are shown by open symbols. These points have been scaled by a factor of 2 for better comparison.

Systematic uncertainties connected with the chosen cross section model have been checked by using different modifications of the model parameters and additionally by checking different FSI modifications of the model. For all targets the

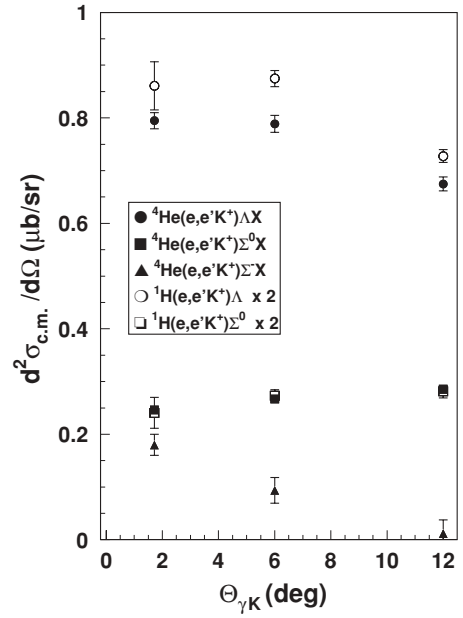

FIG. 9. Same as Fig. 8, but for ^{4}He targets. scaled by a factor of 2 for better comparison.

TABLE V. Missing relative strength in low-mass Λ region, integrated up to the lowest lying Σ^0 threshold. These values were obtained for the choice of our cross section model Eqs. (9)–(13) and Nijmegen *YN* potential as discussed in the text.

Target	$\langle 1.7^\circ \rangle$	1.7°	6°	12°
^{2}H	0.3%	0.3%		
^{3}He	0.7%	2.3%	3%	8%
^{4}He	5%	6%	7%	18%
^{12}C	22%			

values obtained with the model are very stable against small variations in the 3–6% range. Conservatively, we estimate model-dependent uncertainties to be within 6%.

Figures 4 and 7 show some missing strength of the fit in the Λ region for $A = 3, 4, 12$. Integrating the data as well as the fit in the low M_X region below the Λ threshold up to the Σ^0 threshold gives an estimate of the relative missing strength. Nevertheless, we assume that our modeling of the pure quasifree interaction is correct and that this additional strength is due to FSI not described properly by our ERA; we thus assume that this additional strength will not modify the extracted cross section for the quasifree production on these targets. We estimated that at most 1/3 of the percentage of missing strength tabulated in Table V should be added to the systematic uncertainties of the cross section values of Table III.

We checked the systematic uncertainty induced by the choice of a particular *YN* interaction potential within the ERA applied. Again, we see strong dependences on the angle for either target. As an example, the quasifree ^{4}He$(e, e'K^+)\Lambda$ cross section changes by 5% to 6% if the Nijmegen 97f or the Jülich A hyperon nucleon potential are used within the above-mentioned effective range ansatz. This change of the cross section then influences the extraction of the quasifree ^{4}He$(e, e'K^+)\Sigma^0$ cross section by +2.7% to −2.6%, respectively. Values for Λ and Σ^0 do not show a strong angle dependence here; values for the $A = 2, 3$ targets are in similar range. Introducing the final state interaction for the Σ^-, however, may change the cross section for Σ by up to 100% of the value obtained without using the final state interaction. However, the fits without the final state interaction are of far lesser quality than the ones including the final state interaction. We, therefore, do not consider them in Table III.

V. EFFECTIVE PROTON NUMBER

Following Ref [6], an effective proton number Z_{eff} may be obtained by comparing the nuclear with the elementary cross section for Λ production:

$$\left(\frac{d^2\sigma}{d\Omega}\right)_A = Z_{\text{eff}} \left(\frac{d^2\sigma}{d\Omega}\right)_{\text{H}}. \tag{25}$$

In this ansatz, we have to correct for final state interaction by dividing the cross sections by the respective enhancement factors of Table II. If we restrict ourselves to normalizing the respective Λ distribution for the nuclear targets by the Λ distribution from hydrogen, i.e., $Z_{\text{eff}} \simeq \sigma_\Lambda(A)/\sigma_\Lambda(^1\text{H})$, we obtain for the near parallel kinematics and full ϕ coverage, the effective proton numbers given in Table VI. For helium, these numbers are in nice agreement with phenomenological estimates of the respective effective proton numbers that are derived with a procedure similar to that presented in Ref. [10]. The authors of Ref. [10] determine the effective proton number in photoproduction of Λ hyperons on carbon via an eikonal approximation, where the thickness function T is taken to be a harmonic oscillator wave function. The integral [Eq. (22) of Ref. [10]]

$$Z_{\text{eff}} = \frac{\pi}{2} \int dx\, T(x) \exp\left[-\frac{\sigma^{\text{tot}}_{\gamma N} + \sigma^{\text{tot}}_{KN}}{2} T(x)\right] \tag{26}$$

may then be calculated analytically, using $\sigma^{\text{tot}}_{\gamma N} = 0.2$ mb and $\sigma^{\text{tot}}_{KN} = 12$ mb. Using only s waves, Eq. (26) furthermore reduces to

$$Z_{\text{eff}} = a\left[1 - \exp\left(-\frac{Z}{a}\right)\right], \qquad a = \frac{\pi b^2}{\sigma}, \quad \sigma = \sigma^{\text{tot}}_{\gamma N} + \sigma^{\text{tot}}_{KN}, \tag{27}$$

$$T(x) = \frac{2Z}{\pi b^2} \exp\left(-\frac{x}{b^2}\right). \tag{28}$$

For estimating the effective proton number for our targets, we take the following approach. For ^{4}He, we take the rms charge radius of ^{4}He from the literature and fit parameter $b = 1.32$ fm^2. For ^{3}He, we extrapolate the fit parameter b from the values from ^{4}He. For carbon, the values of Ref. [10] are used. Note that using Eq. (27), i.e., not taking into account p-wave contributions for carbon, would yield an effective proton number of 4.0 instead of 4.1. Table VI summarizes our estimates and experimentally derived values. For the deuteron, we also estimated Z_{eff} by using a Hulthén wave function for the deuteron,[3]

$$\psi(r) = \frac{u(r)}{r}, \quad u(r) = N(e^{-\alpha r} - e^{-\beta r}), \tag{29}$$

TABLE VI. Effective proton numbers derived from the cross section in Table III and estimates of effective proton numbers, derived from the calculated absorption taking rms charge radii from literature and other references, cf. text. The superscript * denotes a harmonic oscillator function. Values are given for data at 1.7°, averaged over the azimuth.

Target	rms (fm)	b (fm)	Z	$Z^{\text{exp}}_{\text{eff}}$	$Z^{\text{est}}_{\text{eff}}$
^{2}H	2.140 [41]	(1.71*)	1	0.85 ± 0.09	0.89 (0.93*)
^{3}He	1.976 [42, 43]	1.58	2	1.76 ± 0.16	1.7
^{4}He	1.647 [42, 43]	1.32	2	1.61 ± 0.16	1.6
^{12}C	2.483 [10]	1.64	6	5.15 ± 0.7	4.1

[2] T. S. H. Lee, private communication.
[3] A. Titov, private communication.

$$N = \sqrt{\frac{\alpha\beta(\alpha+\beta)}{2\pi(\alpha-\beta)^2}},$$
$$\alpha = 0.2316\,\mathrm{fm}^{-1}, \quad \beta = 1.268\,\mathrm{fm}^{-1}, \tag{30}$$

for which we obtain $Z_{\mathrm{eff}}^{D} \simeq 0.88$ by numerically integrating Eq. (26).

The overall results are in fair agreement with the estimated values. The value for carbon seems a bit high, but this probably reflects the rather poor statistics of carbon and the difficulty of modeling the cross section and FSI in heavier nuclei.

VI. DEEPLY BOUND KAONIC STATES

From kaon physics many indications have been reported that the $\bar{K}N$ nuclear potential is attractive [44–46]. Predictions of the depths of such potentials vary, as does the possibility of producing deeply bound kaonic states in nuclei. Predictions conclude that such a system should have a drastically contracted core with simple core radius roughly 1/2 of the normal core size, i.e., without the bound $\bar{K}$. It is suggested that a kaonic nuclear system, e.g., $K^- ppn$ would decay into Λpn via the $K^- pp(n) \rightarrow \Lambda p(n)$ and a $\Lambda^*(1405)$ doorway state. The decay products should be visible in several reactions [47], among which also is electroproduction on light nuclei.

Recently, several groups have searched for these states in light nuclei. Such states, Refs. [47–51], are predicted to imply potential depths of $\sim$100 MeV and more while showing small widths of $\sim$10–60 MeV. Some experimental evidence was reported from ^{4}He(stopped K^-, p) experiments at Koo Energy Ken (KEK), the High Energy Research Accelerator Organization in Tsukuba, Japan [52,53], from in-flight $^{16}\mathrm{O}(K^-, n)$ experiments at the BNL Alternating Gradient Synchrotron (AGS) [54], as well as from the FINUDA experiment at DAΦNE [55] in $pp \rightarrow \Lambda p$ invariant mass spectroscopy. For a criticism of the interpretation of these data as bound kaonic states, see Ref. [56]. Moreover, in a recent publication [57], a width estimate, obtained by means of a Faddeev calculation for a $K^- pp$ quasibound state, is of the order of 90–110 MeV, a result at variance with the results of the FINUDA experiment [55].

Experiment E91-016 may access inclusive distributions of final states which may be decay channels of the presumed bound states (cf. Ref. [50]) for $A = 2$: $p + \Lambda, n + \Lambda$; $A = 3$: $p + p + \Lambda, d + \Lambda$; $A = 4$: $\Lambda + t, \Lambda + {}^3\mathrm{He}$. Taking the values of the presumed states from Ref. [47] and comparing with Figs. 4 and 7, we find that for $A = 2$, we are very much at the edge of the acceptance ($M_{ppK^-} \sim 2.32$ GeV), whereas for $A = 3$ ($M_{pppK^-} \sim M_{ppnK^-} \sim M_{pnnK^-} \sim 3.1$ GeV), the presumed states are well within the acceptance, and for $A = 4$, we also should be within the acceptance ($M_{pppnK^-} \sim M_{ppppK^-} \sim 4.13$ GeV). However, while we do expect to have sensitivity within our acceptance for the $A = 3, 4$ cases, the M_X distributions for all nuclei are well described by our model of quasifree kaon production from nucleons distributed according to a theoretical spectral function. Our experiment does not show evidence for deeply bound kaonic states visible in electroproduction, as was proposed in Ref. [50].

VII. SUMMARY

This paper presented for the first time results on the cross section, angular distributions, and nuclear dependence of kaon electroproduction from hydrogen, deuterium, helium-3, helium-4, and carbon. As a result, we obtain quasifree distributions for the respective Λ, Σ^0, and Σ^- hyperons, which are reconstructed by missing mass techniques. These quasifree angular distributions show a behavior similar to the distributions obtained on the free proton. For the extraction of the respective cross sections, the dedicated simple model that was used gave the best description of the data over the kinematic range of the experiment. The extraction of cross sections relied on three decisive steps: using a model developed for the electroproduction of open strangeness on the free proton; employing this model for the description of the quasifree process on nuclei; and using spectral functions convolved with the elementary model. Moreover, it is mandatory to include the final state interaction in the vicinity of the respective thresholds for the production of Λ, Σ^0, and Σ^-. Final state interactions are modeled by an effective range approximation using hyperon nucleon potentials. For carbon, we clearly see the $^{12}_{\Lambda}\mathrm{B}$ bound state, which we do not resolve further, but for which we give a cross section estimate.

Effective proton numbers are extracted by comparing the nuclear cross section with the cross section on the free proton. Correcting for the final state interaction, we see the measured nuclear effects for $A = 2, 3, 4$ in accordance with estimates using a simple eikonal approximation. For carbon, our numbers are higher than the estimated effective proton numbers, which might be due to the small data set at hand.

The missing mass distributions for helium do not show any noticeable structures in the vicinity of $M_X \sim 3.1$ GeV for ^{3}He or $M_X \sim 4.13$ GeV for ^{4}He such that no supportive evidence for deeply bound kaonic states may be drawn from these distributions. It should be pointed out again that these measurements are inclusive and that an exclusive measurement may still have more power in making a statement on these postulated bound states.

Electroproduction experiments with high intensity beams on light nuclear targets are a fascinating subject, which will be studied further at Jefferson Laboratory [58] and the Mainz Microtron (MAMI-C) [59].

ACKNOWLEDGMENTS

We would like to thank Dr. T. S. H. Lee, Dr. A. Titov, and Dr. H.-W. Barz for helpful discussions and support on calculating the effective proton numbers. The excellent support of the staff of the Accelerator and Physics Division of JLab is gratefully acknowledged. F.D. also acknowledges the support of the A.v.Humboldt-Stiftung and the support of ANL for hosting this research. This work was supported in part by the U.S. DOE under Contract Nos. DE-AC03-06CH11357 (ANL) and DE-AC05-84ER40150 (JLab) and by the National Science Foundation.

[1] F. Dohrmann, Int. J. Mod. Phys. E **15**, 761 (2006).
[2] H. Kohri *et al.*, Phys. Rev. Lett. **97**, 082003 (2006).
[3] I. Niculescu (CLAS Collaboration), presented at the International Nuclear Physics Conference INPC2001, Berkeley, CA, July 29–August 3, 2001, nucl-ex/0108013.
[4] A. Boyarski *et al.*, Phys. Rev. D **14**, 1733 (1976).
[5] D. J. Quinn, J. P. Rutherfoord, M. A. Shupe, D. J. Sherden, R. H. Siemann, and C. K. Sinclair, Phys. Rev. D **20**, 1553 (1979).
[6] H. Yamazaki *et al.*, Phys. Rev. C **52**, R1157 (1995).
[7] W. L. Hinton (JLAB E93-018 and E91-016), Nucl. Phys. **A639**, 205c (1998).
[8] T. Miyoshi *et al.* (HNSS), Phys. Rev. Lett. **90**, 232502 (2003).
[9] L. Yuan *et al.* (HNSS), Phys. Rev. C **73**, 044607 (2006).
[10] T. S. H. Lee, Z.-Y. Ma, B. Saghai, and H. Toki, Phys. Rev. C **58**, 1551 (1998).
[11] F. Dohrmann *et al.* (JLab E91-016), Phys. Rev. Lett. **93**, 242501 (2004).
[12] R. M. Mohring *et al.*, Phys. Rev. C **67**, 055205 (2003).
[13] D. Gaskell *et al.*, Phys. Rev. C **65**, 011001 (2002).
[14] D. Dutta *et al.* (JLab E91-013), Phys. Rev. C **68**, 064603 (2003).
[15] P. Ambrozewicz *et al.* (JLab E91-016), Phys. Rev. C **70**, 035203 (2004).
[16] B. Zeidman *et al.*, Nucl. Phys. **A691**, 37 (2001).
[17] G. Knöchlein, D. Drechsel, and L. Tiator, Z. Phys. A **352**, 327 (1995).
[18] S. Janssen, Ph.D. thesis, Universiteit Gent, 2002.
[19] J. C. David, C. Fayard, G. H. Lamot, and B. Saghai, Phys. Rev. C **53**, 2613 (1996).
[20] J. Cha, Ph.D. thesis, Hampton University, 2000.
[21] J. Reinhold *et al.*, Nucl. Phys. **A684**, 470c (2001).
[22] P. Brauel *et al.*, Z. Phys. C **3**, 101 (1979).
[23] C. J. Bebek *et al.*, Phys. Rev. D **15**, 594 (1977).
[24] D. M. Koltenuk, Ph.D. thesis, University of Pennsylvania, 1999.
[25] D. Abbott *et al.* (JLab E91-016), Nucl. Phys. **A639**, 197c (1998).
[26] A. Boyarski *et al.*, Phys. Lett. **B34**, 547 (1971).
[27] R. Ent, B. W. Filippone, N. C R. Makins, R. G. Milner, T. G. O'Neill, and D. A. Wasson, Phys. Rev. C **64**, 054610 (2001).
[28] G. Cowan, *Statistical Data Analysis* (Clarendon, Oxford, UK, 1998).
[29] O. Benhar, A. Fabrocini, S. Fantoni, and I. Sick, Nucl. Phys. **A579**, 493 (1994).
[30] R. Machleidt, K. Holinde, and C. Elster, Phys. Rep. **149**, 1 (1987).
[31] R. B. Wiringa, V. G. J. Stoks, and R. Schiavilla, Phys. Rev. C **51**, 38 (1995).
[32] J. Gillespie, *Final State Interactions* (Holden-Day, San Francisco, 1964).
[33] K. M. Watson, Phys. Rev. **88**, 1163 (1952).
[34] A. B. Migdal, Sov. Phys.-JETP **1**, 2 (1955).
[35] R. G. Newton, *Scattering Theory of Waves and Particles* (Springer, New York, 1982).
[36] X. Li and L. E. Wright, J. Phys. G **17**, 1127 (1991).
[37] T. A. Rijken, V. G. J. Stoks, and Y. Yamamoto, Phys. Rev. C **59**, 21 (1999).
[38] P. M. M. Maessen, T. A. Rijken, and J. J. de Swart, Phys. Rev. C **40**, 2226 (1989).
[39] R. J. Barlow and C. Beeston, Comput. Phys. Commun. **77**, 219 (1993).
[40] A. Uzzle, Ph.D. thesis, Hampton University, 2002.
[41] P. J. M. Mohr, B. N. Taylor, and D. B. Newell, *The 2006 CODATA Recommended Values of the Fundamental Physical Constants*, http://physics.nist.gov/constants (National Institute of Standards and Technology, Gaithersburg, MD, 2007).
[42] C. R. Ottermann *et al.*, Nucl. Phys. **A436**, 688 (1985).
[43] D. Tilley, C. Cheves, J. Godwin, G. Hale, H. Hofmann, J. Kelley, G. Sheu, and H. Weller, *Energy Levels of Light Nuclei, A = 3-20*, http://www.tunl.duke.edu/nucldata/index.shtml (Nuclear Data Evaluation Project, 2007).
[44] C. J. Batty, E. Friedman, and A. Gal, Phys. Rep. **287**, 385 (1997).
[45] F. Laue *et al.* (KaoS Collaboration), Phys. Rev. Lett. **82**, 1640 (1999).
[46] W. Scheinast *et al.* (KaoS Collaboration), Phys. Rev. Lett. **96**, 072301 (2006).
[47] T. Yamazaki and Y. Akaishi, Phys. Lett. **B535**, 70 (2002).
[48] E. Friedman and A. Gal, Phys. Lett. **B459**, 43 (1999).
[49] E. Friedman and A. Gal, Nucl. Phys. **A658**, 345 (1999).
[50] Y. Akaishi and T. Yamazaki, Phys. Rev. C **65**, 044005 (2002).
[51] A. Dote, Y. Akaishi, H. Horiuchi, and T. Yamzaki, Phys. Lett. **B590**, 51 (2004).
[52] T. Suzuki *et al.*, Phys. Lett. **B597**, 263 (2004).
[53] M. Iwasaki *et al.*, nucl-ex/0310018.
[54] T. Kishimoto *et al.*, Nucl. Phys. **A754**, 383 (2005).
[55] M. Agnello *et al.* (FINUDA Collaboration), Phys. Rev. Lett. **94**, 212303 (2005).
[56] E. Oset and H. Toki, Phys. Rev. C **74**, 015207 (2006).
[57] N. V. Shevchenko, A. Gal, and J. Mares, Phys. Rev. Lett. **98**, 082301 (2007).
[58] S. N. Nakamura *et al.* (Jlab E01-011), presented at International Symposium on Electrophoto Production of Strangeness on Nucleons and Nuclei (SENDAI 03), Sendai, Japan, 2003.
[59] J. Pochodzalla, Nucl. Instrum. Methods B **214**, 149 (2004).